

Pharmacological activation of myosin II paralogs to correct cell mechanics defects

Alexandra Surcel^{a,1}, Win Pin Ng^{a,2}, Hoku West-Foyle^a, Qingfeng Zhu^b, Yixin Ren^a, Lindsay B. Avery^c, Agata K. Krenc^d, David J. Meyers^c, Ronald S. Rock^d, Robert A. Anders^b, Caren L. Freel Meyers^c, and Douglas N. Robinson^{a,c,e,1}

Departments of ^aCell Biology, ^bPathology, and ^cPharmacology and Molecular Sciences, Johns Hopkins University School of Medicine, Baltimore, MD 21205;

^dDepartment of Chemical and Biomolecular Engineering, Whiting School of Engineering, Johns Hopkins University, Baltimore, MD 21218; and

^eDepartment of Biochemistry and Molecular Biology, Institute for Biophysical Dynamics, University of Chicago, Chicago, IL 60637

Edited by Robert S. Adelstein, National Heart, Lung, and Blood Institute, National Institutes of Health, Bethesda, MD, and accepted by the Editorial Board December 18, 2014 (received for review July 3, 2014)

Current approaches to cancer treatment focus on targeting signal transduction pathways. Here, we develop an alternative system for targeting cell mechanics for the discovery of novel therapeutics. We designed a live-cell, high-throughput chemical screen to identify mechanical modulators. We characterized 4-hydroxyacetophenone (4-HAP), which enhances the cortical localization of the mechanoenzyme myosin II, independent of myosin heavy-chain phosphorylation, thus increasing cellular cortical tension. To shift cell mechanics, 4-HAP requires myosin II, including its full power stroke, specifically activating human myosin IIB (MYH10) and human myosin IIC (MYH14), but not human myosin IIA (MYH9). We further demonstrated that invasive pancreatic cancer cells are more deformable than normal pancreatic ductal epithelial cells, a mechanical profile that was partially corrected with 4-HAP, which also decreased the invasion and migration of these cancer cells. Overall, 4-HAP modifies nonmuscle myosin II-based cell mechanics across phylogeny and disease states and provides proof of concept that cell mechanics offer a rich drug target space, allowing for possible corrective modulation of tumor cell behavior.

mechanical modulator | 3,4-dichloroaniline | 4-hydroxyacetophenone | myosin II | pancreatic cancer

Cell shape change processes include cell growth, division, motility, and the formation of complex structures like tissues and organs, all of which are governed by the intersection of biochemistry, genetics, and mechanics. These three modules are integral not just for normal function in healthy cells but also in disease states. Pharmacological manipulation of some of these modules has already led to treatment strategies for inflammation and cancer (e.g., paclitaxel) (1, 2). However, many presently available therapies, which address only one aspect of cell shape change, typically either fail to abolish the disease completely or lead to compensatory regulatory changes, and therefore to drug resistance. Targeting cell mechanics remains an underused approach for drug development. In cancer, altered cell mechanics are a hallmark of metastatic efficiency: cell stiffness decreases up to 70% in many metastatic cancer cells (3–5). It is rational then that one therapeutic approach is to increase cellular elasticity, which would, in turn, reduce metastatic potential and act downstream of cancer-inducing genetic alterations.

Known mechanical modulators (e.g., latrunculin, blebbistatin) are often lethal, have numerous off-site targets, and act to generate a softer and metastatic-like mechanical phenotype (6, 7). However, the field's ability to increase cellular elasticity on acute time scales is highly restricted. In an effort to close this gap and find modulators that stiffen cells, we leveraged our molecular and analytical understanding of cytokinesis, an evolutionarily conserved and highly mechanical cell shape change event, to establish an in vivo, large-scale, high-throughput chemical screen for small-molecule modulators of cell shape change. Because our goal was to identify compounds that would provide a correcting function rather than simply killing cells (i.e., do no harm by

minimizing side effects), we searched for highly potent, subtle modulators rather than drugs that would completely abolish cell division. The primary screen was designed to segregate and rank-order hits based on their cytokinesis inhibitory activity, mitotic inhibitory activity, or lethality in *Dictyostelium*, an amoebozoan that undergoes metazoan-type cytokinesis.

Here, we present Chembridge 5180622 (referred to as carbamate-7), which was identified in our pilot screen of over 22,000 compounds. Carbamate-7 is a highly potent cell mechanics modulator that inhibits cytokinesis weakly, as designed by our specific experimental approach. Evaluation of carbamate-7 demonstrated that it inhibits cytokinesis by influencing the RacE/14-3-3/Myosin II (MyoII) pathway, known to regulate cortical mechanics (8). This activity arises not from carbamate-7, but rather from the action of two degradation products: 3,4-dichloroaniline (3,4-DCA) and 4-hydroxyacetophenone (4-HAP). We show that 4-HAP is sufficient to alter the mechanoenzyme myosin II localization and cellular mechanics in a myosin II heavy-chain phosphorylation-independent manner, specifically targeting the myosin II power stroke of the myosin II ATPase cycle. Furthermore, we measured the effect of 4-HAP on several pancreatic cancer cell lines (Pancs). Previous genetic analysis of Pancs supports the hypothesis that the tumor cell's mechanical profile may correlate with disease progression (9). Here, we found that the viscoelasticity of late-stage Pancs is reduced (softer) relative to normal

Significance

Despite the integral role of cell mechanics, efforts to target mechanics for drug development have lagged. Here, we present an approach to identifying small molecules capable of modulating mechanics. We characterize 4-hydroxyacetophenone (4-HAP), isolated as a breakdown product of a hit from our pilot screen of over 22,000 compounds. We show that 4-HAP specifically alters the localization of the mechanoenzyme myosin II, increasing the stiffness of cells. The effect of 4-HAP on myosin II, whose specificity we have defined, occurs across phylogeny. In particular, we have demonstrated 4-HAP's ability to convert the mechanical profile of metastasis-derived pancreatic cancer cells toward a normal WT-like state. Invasion and migration of these cells, which are hallmarks of the invasive capacity of malignant lesions, are decreased by 4-HAP.

Author contributions: A.S., W.P.N., R.S.R., R.A.A., C.L.F.M., and D.N.R. designed research; A.S., W.P.N., H.W.-F., Q.Z., Y.R., L.B.A., A.K.K., D.J.M., and C.L.F.M. performed research; A.S. and D.N.R. analyzed data; and A.S. and D.N.R. wrote the paper.

The authors declare no conflict of interest.

This article is a PNAS Direct Submission. R.S.A. is a guest editor invited by the Editorial Board.

¹To whom correspondence may be addressed. Email: asurcel1@jhmi.edu or dnr@jhmi.edu.

²Present address: Department of Bioengineering, University of California, Berkeley, CA 94720.

This article contains supporting information online at www.pnas.org/lookup/suppl/doi:10.1073/pnas.1412592112/-DCSupplemental.

human pancreatic ductal epithelial (HPDE) cells. Treatment with 4-HAP increases the elasticity of Pancs, converting the cell's viscoelasticity to a more normal HPDE-like state. These mechanical alterations in mammalian cell lines are dependent upon activation of human myosin IIB (MYH10) and human myosin IIC (MYH14), but not human myosin IIA (MYH9). Furthermore, 4-HAP decreases migration and invasion of these metastatic cells in *in vitro* assays.

Results

Carbamate-7 Affects the RacE/14-3-3/MyoII Pathway. We developed a processing and analysis platform called cytokinesis image processing analysis quantification (CIMPAQ) to maximize data collection from a single screen and to perform in-house data analysis. CIMPAQ allows us to analyze high-content imaging data to identify cell viability and cytokinetic and mitotic defects of *Dictyostelium* cells by counting cells, determining the number of nuclei per cell, and measuring the nuclear size, respectively (a complete description outlining the criteria for CIMPAQ hit identification is provided in [Supporting Information](#); also refer to Fig. 1*A* and [Figs. S1 E–I](#) and [S2](#)). To ensure that a full frequency distribution of all of these parameters could be extracted, each sample well contained over 400 cells per time point. This approach led to richer, more statistically relevant datasets compared with those datasets normally collected for high-throughput screens. We developed and used a nuclear reporter [nuclear localization sequence (NLS)-tdTomato] that is optimal for live cell imaging in

normal growth media over multiple time points and allows for the number of nuclei in each cell and nuclear area to be discerned.

Proof-of-principle pilot screens were conducted ([Fig. S2](#) and [Tables S1](#) and [S2](#)) and compared with manual nuclei per cell counts ([Fig. S1G](#)). Over 22,000 compounds from the ChemBridge DIVERSet library were screened using CIMPAQ. Approximately 15% of the screened compounds inhibited cell growth, and 25 affected cytokinesis. Here, we focus on carbamate-7 ([Fig. 1B](#)) treatment, which resulted in an increase in the binucleate-to-mononucleate ratio, as well as in the multinucleate-to-mononucleate ratio (both indicative of mild cytokinesis inhibition), at 6 SDs over untreated cells ([Fig. 1C](#)). A dose sensitivity analysis identified an increase in binucleate cells in the low nanomolar range, suggesting late mitotic or early cytokinesis failure, which became particularly evident at 48 h ([Fig. 1D](#)).

To assess whether carbamate-7 affects known cytokinesis pathways, we targeted two spatially distinct modules, one at the equatorial plane of a dividing cell regulated by spindle signals and the mechanosensory system of Myosin II/Cortexillin I, and one at the polar cortex regulated by the RacE/14-3-3/MyoII pathway (8). In chemical-genetic epistasis analyses, we challenged mutant cell lines targeting both modules with carbamate-7. In the *kinesin 6* (encoded by the *kif12* locus) null cell line, cytokinesis inhibition by carbamate-7 occurred as in WT, suggesting that carbamate-7 affects a parallel cytokinesis pathway independent of the spindle signaling cascade involving kinesin 6. By contrast, carbamate-7 did not increase binucleation or multinucleation in *myoII* and *racE* null cell lines relative to the untreated controls. These results suggest that carbamate-7 likely works through the RacE/14-3-3/MyoII pathway ([Fig. 1E](#)). Epifluorescence and structured illumination microscopy studies of mCherry-racE and GFP-myosin II in their respective rescued cell lines challenged with carbamate-7 revealed no change in racE localization, but a significant increase in GFP-myosin II cortical accumulation ([Fig. 2A](#)). A dose-dependent assessment of carbamate-7 on myosin II localization using total internal reflection microscopy (TIRF) exposed an increase in the myosin II functional unit, the bipolar thick filament (BTF), at the cortex in the range of 500 pM ([Fig. 2B](#) and [C](#)). These results were corroborated with *in vitro* sedimentation assays showing an increase in the BTF-containing Triton X-100-insoluble fraction ([Fig. 2D](#)). Because myosin II is a known effector of cell mechanics, both in *Dictyostelium* as well as in other organisms (8, 10–14), we next queried whether the increase in cortical localization would have an impact on the mechanical properties of the cell. Using micropipette aspiration (MPA) assays, we determined that acute treatment with 700 pM carbamate-7 led to a 1.4-fold increase in the cell's cortical tension ([Fig. 2E](#)), providing direct evidence that our screen successfully identified a modulator of cell mechanics.

Carbamate-7 Chemistry. The hit 5180622 (carbamate-7) was described as 4-acetylphenyl(3,4-dichlorophenyl) carbamate in the ChemBridge DIVERSet library. To validate the identity and activity of the putative carbamate-7, we synthesized and characterized an authentic sample of 4-acetylphenyl(3,4-dichlorophenyl) carbamate from 4-HAP and 3,4-dichlorophenyl isocyanate ([Fig. S3A](#)). Interestingly, the carbamate was unstable during purification, raising questions about its stability in the ChemBridge DIVERSet library. HPLC analysis to assess the stability of the carbamate in DMSO showed complete conversion of the carbamate to two major products, 3,4-DCA and 4-HAP, within 15 min ([Fig. S3B](#)). *N,N'*-Bis(3,4-dichlorophenyl)urea also appeared as a minor degradation product in DMSO. Stock solutions of carbamate-7 were subsequently analyzed and found to contain a mixture of 4-HAP, 3,4-DCA, and the urea ([Fig. 3A](#)). No 4-acetylphenyl(3,4-dichlorophenyl) carbamate could be detected in the commercial stock solutions.

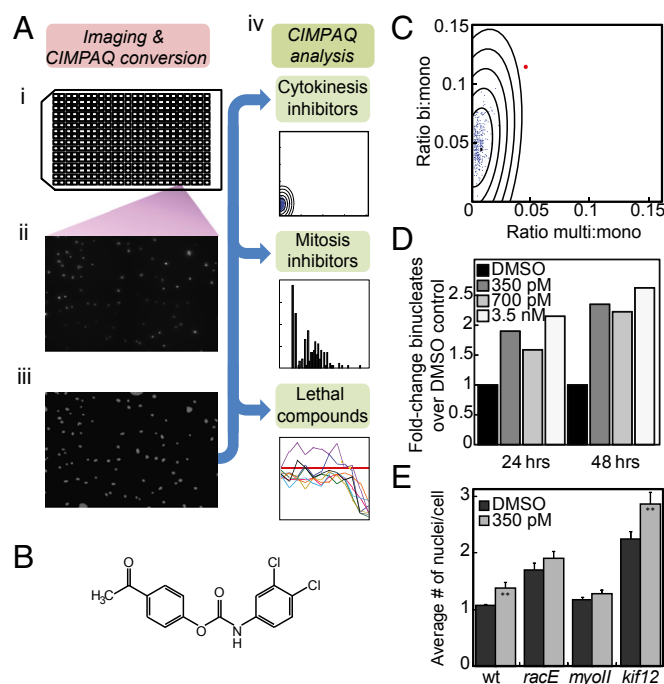


Fig. 1. ChemBridge identification no. 5180622 (carbamate-7) is identified as a cytokinesis inhibitor affecting the Myosin II/RacE pathway. (A) Primary screening work flow includes (i) plating; (ii) raw data acquisition; (iii) CIMPAQ image conversion; and (iv) rank ordering of cytokinesis inhibitors, mitotic inhibitors, and lethals. (B) Carbamate-7 structure. (C) Well with carbamate-7-treated cells (red) showed a shift in the nuclei per cell distribution compared with the DMSO control (blue) by CIMPAQ analysis. SD lines represent SD2–SD6. (D) Partial dose-response curves reveal an increase in binucleates at nanomolar concentrations ($n = 1,000$ – $4,000$ cells per condition). (E) Chemical-genetic epistasis analysis indicates that carbamate-7 affects the RacE/14-3-3/MyoII pathway. To normalize across cell lines with varying degrees of cytokinesis defects, the average number of nuclei per cell is plotted. Error bars represent SEM. $**P < 0.0001$.

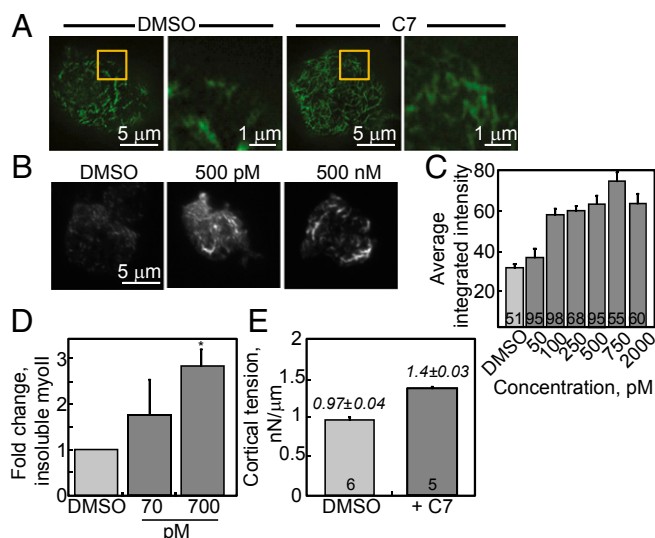


Fig. 2. Myosin II cortical dynamics are affected by treatment with carbamate-7 (C7). (A) Structured illumination microscopy images show an increase in the amount and variability of myosin II BTFs in 500 nM C7-treated (Right) vs. untreated (Left) *myoII::GFP myoII* cells (zoomed-in boxed regions are also shown). TIRF reveals a dose-dependent increase of cortical GFP-myosin II (B), which is quantified (C). The number of cells quantified is shown on bars. (D) Sedimentation assays show an increase of nonmonomeric myosin II (insoluble fraction) in 700 nM C7-treated vs. untreated WT cells ($n = 3$). $*P = 0.02$. (E) Cortical tension measurements show a 1.4-fold increase in cells treated for 15 min with C7. Error bars represent SEM. The number of cells quantified is shown on bars.

Small Molecule 4-HAP Works Through Myosin II. Because the degradation products arising from carbamate-7 appeared to be stable for >24 h at 22 °C, studies were carried out to determine which of these components displayed the biological activity identified above. We show with nuclei per cell distributions over a concentration range from 500 pM to 5 μM, that none of the degradation products alone is sufficient for cytokinesis inhibition but that a 1:1 combination of 3,4-DCA and 4-HAP increased binucleation 2.5-fold over control cells (Fig. 3B, full curve is illustrated in Fig. S3D). We then analyzed the cortical enrichment of myosin II in cells treated with each compound and found that 4-HAP alone drives myosin II relocalization (Fig. 3C and D). These results imply that we have identified a compound combination that works on two separate yet related pathways involved in cytokinesis.

To gauge the time dependency of the myosin II cortical accumulation, we performed time-course experiments using TIRF microscopy. When challenged with 4-HAP, myosin II BTFs accumulate at the cortex within 5 min, reaching steady state at 15 min (Fig. 3E and F). In a majority of cells, the BTF structures increase in length and intensity, whereas in a subset of cells (~15%), they accumulate into ribbon-like rings (Fig. 3E). This 2.5-fold increase in myosin II at the cortex is fully reversible (Fig. S4) and is not the result of changes in the contact area of the cells (Figs. S4 and S5). Neither 3,4-DCA nor the urea results in changes in myosin II cortical distribution (Fig. S5). We next asked if the 4-HAP-induced myosin II shift was responsible for the mechanical changes we had observed previously. WT cells challenged with 4-HAP displayed a 1.5-fold increase in cortical tension compared with untreated cells, whereas 3,4-DCA had no effect. The change in cortical tension is dependent on myosin II, because *myoII* null cells did not experience a similar shift in mechanics (Fig. 3G).

Myosin II BTF formation is regulated by the enzymatic conversion of myosin II monomers from assembly-incompetent to assembly-competent forms, resulting in their dimerization and further assembly into functional BTFs (15, 16). This conversion

is driven by the dephosphorylation of three threonines in the myosin tail of the heavy chain, all of which are C-terminal to the assembly domain (17, 18). To determine if 4-HAP activation of myosin II impinges on this assembly scheme, we tested the effect of 4-HAP on the *in vivo* assembly dynamics of the assembly-incompetent phosphomimetic form of myosin (3XAsp), as well as the assembly-over-competent unphosphorylatable form (3XAla), in *myoII* null cells (17–19). Both cell lines showed an increase in filament formation compared with their controls at 10 min posttreatment, with 3XAsp generating more short filaments and 3XAla increasing in filament length and intensity (Fig. 4A and B and Fig. S6). To investigate the role of the assembly domain of myosin in 4-HAP activation further, we performed *in vitro* assembly assays on a myosin II tail fragment, assembly domain C-terminal, which is sufficient to reconstitute regulatable myosin II BTF assembly, as well as on tail fragments from MYH9 and

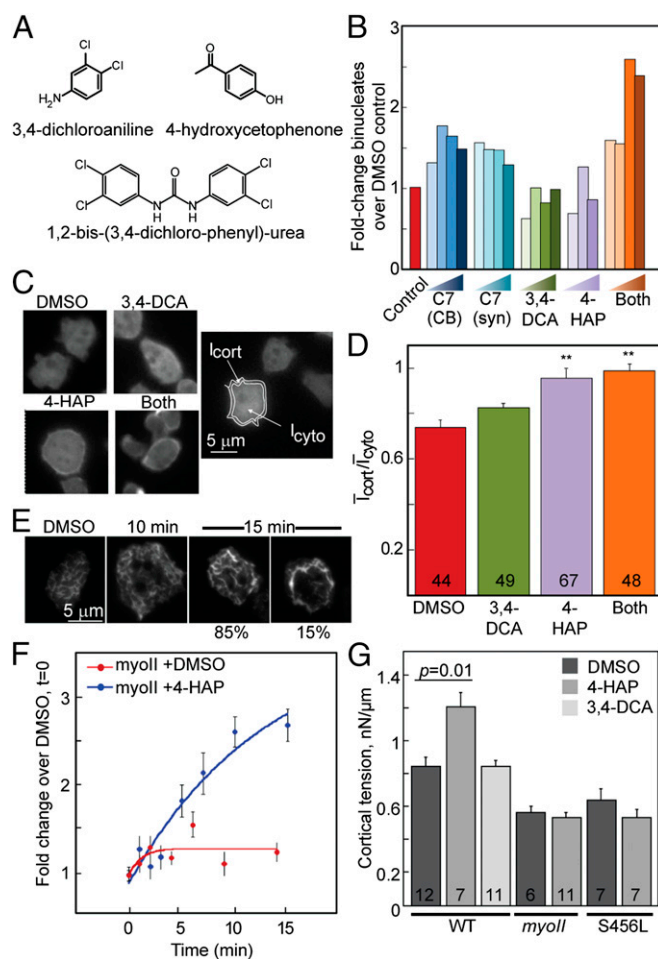


Fig. 3. 4-HAP, a degradation product of C-7, activates myosin II-mediated mechanics. (A) C7 breakdown product structures. (B) Both 3,4-DCA and 4-HAP are required for the binucleation increase seen with C7 treatment. CB, ChemBridge; syn, synthesized. Compound concentrations: 1 nM, 500 nM, 1,000 nM, and 5,000 nM. The 5,000 nM 4-HAP concentration was lethal, and is therefore not shown ($n = 400$ – $1,441$ cells per condition). (C) Epifluorescence micrographs show that 4-HAP and a 1:1 mixture (Both) enrich cortical myosin II. (D) Cartoon illustrates the quantification method of cortex/cytoplasm intensity ratios. Cell numbers are shown on bars. $**P = 0.005$. (E) TIRF images show cortical GFP-myosin II BTF enrichment upon 500 nM 4-HAP treatment. The population distribution is indicated. (F) GFP-myosin II accumulates within 10 min of 4-HAP treatment. (G) 4-HAP 500 nM concentration increases cortical tension in a myosin II-dependent manner. Cell numbers are shown on bars. Error bars represent SEM.

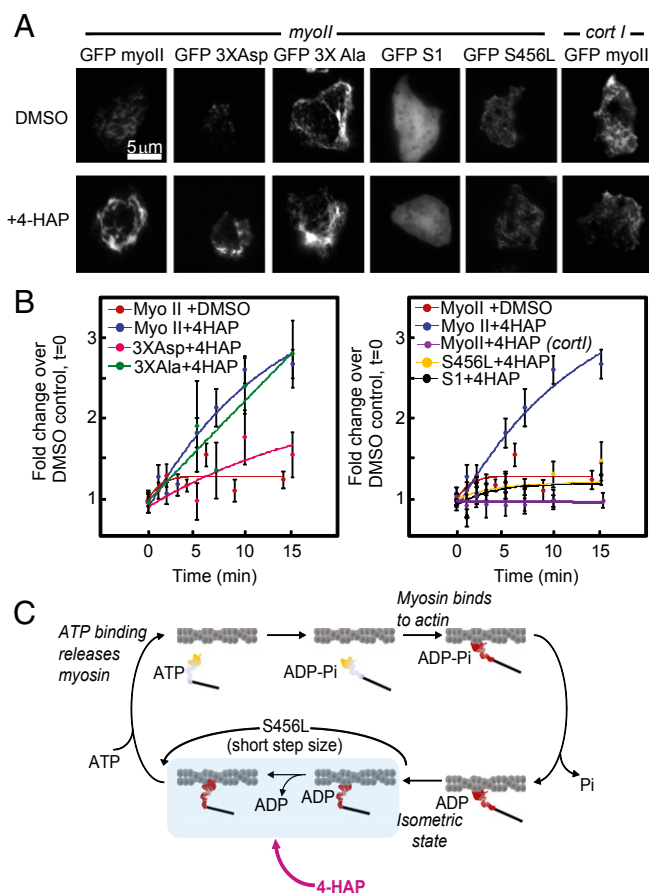


Fig. 4. Myosin II activation by 4-HAP is independent of myosin II heavy-chain phosphorylation but requires the normal power stroke. (A) TIRF images of GFP-myosin II, 3XAsp, and 3XAla expressing *myoII* null cell lines in DMSO vs. 500 nM 4-HAP treatment show an increase in cortical BTfs at 15 min after addition. (B) 4-HAP time-course quantification. Similar treatment of GFP-S1- and GFP-S456L-expressing *myoII* null cell lines and GFP-myosin II in the *cortI* null cell line showed no change (A) over the time course of the experiment (B, Right) ($n = 17-42$). (C) Cartoon indicates that to have an effect on myosin's localization, 4-HAP requires myosin II to take a full power stroke. Treatment with 4-HAP does not promote accumulation of S456L, which only takes a 2-nm step, one-quarter of the WT step (20).

MYH10. These experiments were also conducted in the presence or absence of 14-3-3, a myosin II-binding partner that sequesters free myosin monomers, thus increasing the sensitivity of the assembly assay and providing a positive control for a direct effector of myosin II assembly (8). In all experimental setups, 4-HAP did not affect the assembly of myosin II, including the MYH9 and MYH10 paralogs (Fig. S7A–C). These overall results imply that BTF assembly in the presence of 4-HAP is independent of myosin II heavy-chain phosphorylation. Therefore, 4-HAP-induced cortical accumulation of myosin BTfs may be caused by alterations to other parts of the myosin recruitment pathway or to the myosin II ATPase cycle.

To test the latter hypothesis, we used the myosin mutant S456L. The S456L mutation disrupts the communication between the motor's ATP-binding pocket and converter domain, resulting in normal ATPase activity but a 10-fold slower actin filament sliding velocity (20). Unlike the assembly-compromised myosin mutants, *myoII* null cell lines complemented with GFP-S456L did not show a response to 4-HAP, even when the time course was extended beyond 1 h (Fig. 4A and B and Fig. S6). Additionally, *myoII::GFP-S456L* cells did not have a change in

cortical tension when treated with 4-HAP (Fig. 3G). These data highlight a highly restrictive target space for 4-HAP in the myosin II mechanochemical cycle. Further, the myosin II motor domain alone (subfragment 1-S1) of myosin II did not show an accumulation response to 4-HAP treatment, indicating that 4-HAP's effect requires dimeric myosin II or fully assembled BTfs and was not simply altering the energy state of the cell (Fig. 4A and B). These results indicate that 4-HAP requires the full myosin II power stroke (Fig. 4C and SI Discussion). We tested whether 4-HAP could affect the in vitro motility of mammalian myosin IIB and found that 4-HAP did not significantly alter this myosin's motility (Fig. S7D). However, in vitro motility assays only probe the rate-limiting step for motility under no-load conditions. In vivo, myosin II experiences load in the context of a mechanosensory control system anchored, in part, by its co-operative interaction with another actin cross-linker, cortexillin I (21, 22). If we interrupt this control system by deleting cortexillin I, 4-HAP-directed myosin II accumulation is also abolished (Fig. 4A and B and Fig. S7E and F). These results reveal that 4-HAP requires normal genetic pathways for myosin II accumulation to occur.

Small Molecule 4-HAP Stiffens Pancreatic Cancer Cells and HEK 293 Cells but Not HL-60 Cells.

Pancreatic intraepithelial neoplasia (PanIN) that progress toward pancreatic ductal adenocarcinoma (PDAC) contain a few key genetic lesions that disproportionately affect key cytoskeletal regulators and players. For example, 95% of PDACs have early activating mutations in *Kras*, which modulates cell elasticity (23, 24). Early PanINs also up-regulate the actin cross-linking protein fascin, whereas later stages are marked by the up-regulation of 14-3-3 σ , a regulator of myosin II assembly (8, 25, 26). Furthermore, serial analysis of gene expression of numerous Pans that were compared with normal pancreatic cells (HPDE cells) revealed alterations in the expression of several regulators of myosin II assembly and contractility (9). Based on these observations, we hypothesized that PDAC progression might be correlated with changes in cellular mechanics and, furthermore, that if these mechanics are myosin II-driven, they might be restored to normal, healthy mechanical profiles with 4-HAP.

To test this hypothesis, we performed MPA experiments on WT-like HPDE cells and two patient-derived Pans: A10.7, a liver-derived metastatic PDAC cell line, and the commonly used ASPC-1, an ascites-derived metastatic PDAC cell line (9, 27). Creep tests demonstrated that these cell lines are mechanically distinct: HPDE cells are significantly stiffer than ASPC-1 or A10.7 cells. The addition of 4-HAP (500 nM or 50 μ M) increased the elastic nature of both PDAC cell lines, returning them to an HPDE-like profile (Fig. 5D and E and Fig. S7G). Treatment with 4-HAP had a similar effect on the widely used human kidney-derived HEK 293 cells (Fig. 5A and B). As in *Dictyostelium*, 4-HAP affects myosin II assembly in human-derived cell lines: sedimentation assays showed an increase in myosin IIC BTF formation, whereas the myosin IIA paralog and the myosin IIA tail phosphosite (phospho-Ser1943) showed little change (Fig. 5C and F and Fig. S7H and I). Myosin IIB also showed a shift in assembly in response to 4-HAP in HEK 293 (Fig. 5C) but not in HPDE (Fig. S7H) cells. In contrast, ASPC-1 cells had no detectable myosin IIB. Due to the myosin II paralog specificity of 4-HAP in these cell lines, we next asked whether 4-HAP affects the mechanical profile of human promyelocytic leukemia (HL-60) cells, which solely express myosin IIA. Treatment with 4-HAP did not affect the cortical tension of these cells (Fig. 5G), further implying paralog specificity. Additionally, 4-HAP had no dose-response effect on ASPC-1 viability (Fig. S7J).

Because the initial premise of our original screen was that small molecules that modulate mechanics can affect cancer mechano-behaviors, we tested the invasive capacity of 4-HAP-treated cells. ASPC-1 cells treated with 4-HAP show a dose-dependent

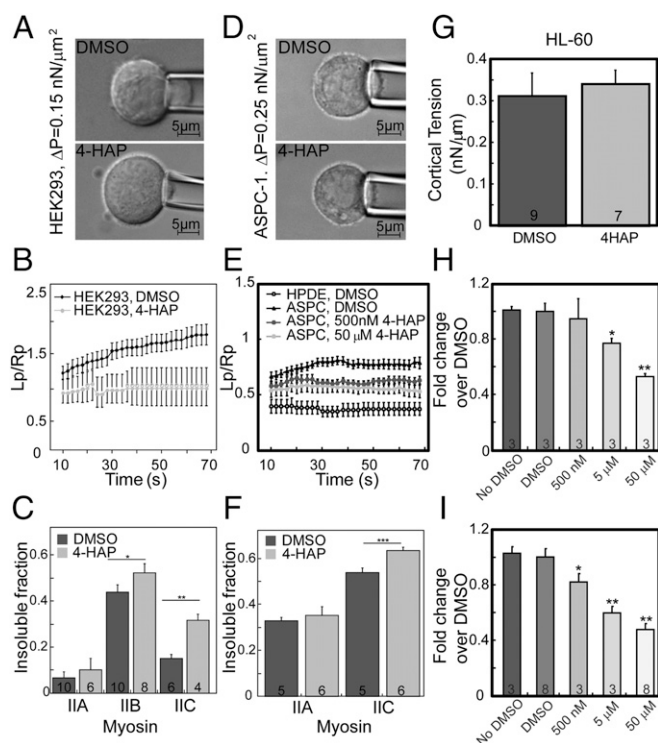


Fig. 5. 4-HAP decreases the deformability of human cells and tunes the mechanical profile of pancreatic cancer cells to more WT-like mechanics, decreasing their invasive capacity. Micrographs (A) from creep tests (B) show that 500 nM 4-HAP stiffens the soft HEK 293 cells (creep tests at 0.15 nN/ μm^2). Lp, region of aspiration; Rp, radius of pipette. (C) Sedimentation assays show increases in assembled myosin IIB and myosin IIC in HEK 293 cells. $*P = 0.04$; $**P = 0.007$. (D) Similarly, micrographs of aspirated cells show that 500 nM 4-HAP tunes the deformability of metastatic PDAC ASPC-1 cells. (E) Creep tests demonstrate that the WT pancreatic cell line HPDE is stiffer than the metastatic PDAC cell line ASPC-1 and that 4-HAP stiffens ASPC-1 cells, shifting them toward HPDE-like mechanics (creep tests at 0.25 nN/ μm^2). (F) Concentration of 4-HAP at 500 nM increases assembled myosin IIC in ASPC-1 cells and HPDE cells (Fig. S7H). Cell numbers are shown on bars. $***P = 0.005$. (G) 4-HAP does not alter the cortical tension of HL-60 cells, which lack the myosin IIB and myosin IIC paralogs. All experiments presented here were performed using cells treated with 4-HAP for 1 h. Migration (H) and invasion (I) assays of ASPC-1 cells show a dose-dependent decrease upon 4-HAP treatment. Cell numbers are shown on bars. $**P < 0.0001$; $*P = 0.01$ for migration assay; $*P = 0.02$ for invasion assay.

decrease in in vitro migration and invasion, with a modest, but significant inhibition at 500 nM and more significant inhibition at 5 and 50 μM (Fig. 5 H and I). These results suggest that the mechanical stiffening triggered by 4-HAP is sufficient to reduce the invasive capacity of metastasis-derived PDAC cells. Collectively, these results demonstrate 4-HAP's ability to alter cellular mechanics across phylogeny and disease states.

Discussion

The behavior and decision making of cells and entire tissues are derived, in large part, from their mechanical makeup and microenvironment. Cell mechanics define how the cell responds to its microenvironment and how it is able to display behaviors, such as tissue invasion or tumor dissemination. Myosin II has long been ascribed tremendous importance in maintaining the mechanical integrity of cells. As a mechanoenzyme, nonmuscle myosin II is pivotal in an extensive array of normal physiological mechanosensation and mechanotransduction processes, including cell division, adhesion, motility, stem cell differentiation, and tissue morphogenesis. Mutations in myosin II paralogs and myosin II regulatory proteins are associated with a number of

diseases, such as the MYH9-related disease cluster (May–Hegglin anomaly, Epstein syndrome, and Sebastian syndrome) (28–30). Increasingly, altered nonmuscle myosin II regulation is correlated with tumor progression and metastasis: The up-regulation of Kras, 14-3-3, and Rac signaling leads to down-regulation of contractile myosin II (8, 24, 31–35). These changes in expression, often caused by genetic lesions, can provide a mechanical differential, giving precancerous cells an advantage over their neighbors in breast and pancreatic cancer progression (23, 25, 26).

Affecting myosin II activity along the cellular mechanics continuum—whether through a direct disruption of myosin II-cofactor complexes or a shift in the myosin II-mediated cooperative interactions that respond to mechanical stress (36, 37)—has enormous therapeutic potential. Here, we demonstrate the ability to identify small molecules that affect known mechano-sensitive pathways by targeting the mechanical process of cell shape change that occurs during cytokinesis. We have identified 3,4-DCA and 4-HAP, the latter of which alters myosin II-dependent cell mechanics. We further demonstrate that fine-tuning myosin IIB and myosin IIC dynamics can mechanically stiffen Panes toward a more WT mechanical profile, which in turn alters the migration and invasion of these cells (Figs. 4 and 5). Our strategy for identifying and characterizing small-molecule modulators has broad implications not just in pancreatic adenocarcinoma but across cancer cell types characterized by mechanical transitions, such as breast and lung cancers (24, 38), as well as other MYH10- and MYH14-based diseases. Indeed, animal studies are required to test the efficacy of 4-HAP for treating a range of these myosin II-based diseases.

Acetophenones, such as 4-HAP, have been previously identified as the chemical and microbial degradation products for a wide array of industrial and agricultural chemicals (39), such as bisphenol-A (40) and 4-(1-nonyl)phenol, where it is used for growth by some aerobic microorganisms (41, 42). In addition, 4-HAP has been isolated from *Cynanchum paniculatum* and *Cynanchum wilfordii* extracts, and is commonly used for its anti-inflammatory and vascular-protective effects (43–45). It will be of interest to explore the possibility that 4-HAP may have an impact on the mechanics of vascular tissue, as well as to expand upon its ability to alter myosin II dynamics in other mammalian cell types, particularly cancer cells. In addition, carbamate-7, the originally identified compound whose degradation leads to these two main byproducts, is part of a family of compounds that includes protham and chlorprotham. These compounds have been used widely in herbicides (46) and were previously classified as mitotic inhibitors, with demonstrated growth defects and alterations in spindle morphology (47–52). Although we found that neither 3,4-DCA nor 4-HAP affected microtubule structure, we have previously demonstrated a link between microtubules and the RacE/14-3-3/MyoII pathway (8). Our studies on 4-HAP and 3,4-DCA may provide further mechanistic insight into the mode of action of this class of compounds. More importantly, 4-HAP provides an important strategy for modulating cell mechanics and will be of interest to test in a wide range of disease processes, as well as in tissue engineering, where cell differentiation may be guided by environmental mechanics.

Methods

Screen Development and CIMPAQ Analysis. NLS-tdTomato-expressing *Dictyostelium* cells were challenged with 5 μM compounds from the ChemBridge DIVERSet library and imaged over 3 d. Raw data were segmented by CIMPAQ, a designed analytical platform, which rank-ordered hits based on their cytokinesis or mitotic inhibitory activity or lethality. Hits were confirmed through a dose-dependent secondary screening.

Cell Culture. *Dictyostelium* strains were grown at 22 °C in Hans' enriched HL-5 media or HL-5 medium with glucose (FORMEDIUM Ltd.), with either G418 or hygromycin for selection. A strain list is provided in Table S3.

Pancreatic cell lines HPDE, A10.7, and ASPC-1 were grown in DMEM, keratinocyte media, or RPMI media with appropriate supplementation.

MPA and Microscopy. MPA was used for cortical tension and creep response measurements. Confocal imaging was performed on a Zeiss 510 Meta microscope with a 63 \times (1.4 N.A.) objective (Carl Zeiss). Epifluorescence and TIRF imaging was performed in a 22 $^{\circ}$ C temperature-controlled room with an Olympus IX81 microscope using a 40 \times (1.3 N.A.) or 60 \times (1.49 N.A.) objective and a 1.6 \times optovar (Olympus), as previously described. Image analysis was performed with ImageJ software (rsb.info.nih.gov/ij).

In Vitro Protein Assays. Sedimentation assays were used to assess myosin II assembly in cells. The assembly assay used purified proteins (N-terminal 6 \times His tag fused to the mCherry fluorophore) fused to the assembly domains of *Dictyostelium* myosin II (residues 1,533–1,823), MYH9 (residues 1,722–1,960), MYH10 (residues 1,729–1,976), and 6 \times His-tagged fused *Dictyostelium* 14-3-3.

Purified chicken nonmuscle IIB heavy meromyosin was used for in vitro motility.

Chemistry. Carbamate-7 was synthesized from 4-HAP and 3,4-dichlorophenyl isocyanate, and confirmed by NMR. We used HPLC to assess the carbamate-7 breakdown products. The urea was confirmed by MS. Commercial and synthesized carbamate-7 showed identical degradation products.

ACKNOWLEDGMENTS. We thank Yuan Xiong and Peter Devreotes for discussions, Eric Schiffhauer for tissue culture assistance, and Christine Iacobuzio-Donahue for pancreatic cell lines. We thank members of the D.N.R. laboratory for feedback on the manuscript. We acknowledge the Johns Hopkins University ChemCORE Facility for chemical library storage and handling. This work was supported by NIH Grant GM66817 (to D.N.R.), NIH Grant AI099704 (to C.L.F.M.), National Cancer Institute Anti-Cancer Drug Development Training Grant T32 CA009243 (to A.S.), and the Sol Goldman Pancreatic Cancer Center (D.N.R. and R.A.A.).

- Girdler F, et al. (2006) Validating Aurora B as an anti-cancer drug target. *J Cell Sci* 119(Pt 17):3664–3675.
- de Weger VA, Beijnen JH, Schellens JH (2014) Cellular and clinical pharmacology of the taxanes docetaxel and paclitaxel—A review. *Anticancer Drugs* 25(5):488–494.
- Discher DE, Janmey P, Wang YL (2005) Tissue cells feel and respond to the stiffness of their substrate. *Science* 310(5751):1139–1143.
- Bhadriraju K, Hansen LK (2002) Extracellular matrix- and cytoskeleton-dependent changes in cell shape and stiffness. *Exp Cell Res* 278(1):92–100.
- Chiang AC, Massagué J (2008) Molecular basis of metastasis. *N Engl J Med* 359(26):2814–2823.
- Girard KD, Kuo SC, Robinson DN (2006) Dictyostelium myosin II mechanotransduction promotes active behavior of the cortex on long time scales. *Proc Natl Acad Sci USA* 103(7):2103–2108.
- Wakatsuki T, Schwab B, Thompson NC, Elson EL (2001) Effects of cytochalasin D and latrunculin B on mechanical properties of cells. *J Cell Sci* 114(Pt 5):1025–1036.
- Zhou Q, et al. (2010) 14-3-3 coordinates microtubules, Rac, and myosin II to control cell mechanics and cytokinesis. *Curr Biol* 20(21):1881–1889.
- Jones S, et al. (2008) Core signaling pathways in human pancreatic cancers revealed by global genomic analyses. *Science* 321(5897):1801–1806.
- Reichl EM, Robinson DN (2007) Putting the brakes on cytokinesis with alpha-actinin. *Dev Cell* 13(4):460–462.
- Reichl EM, et al. (2008) Interactions between myosin and actin crosslinkers control cytokinesis contractility dynamics and mechanics. *Curr Biol* 18(7):471–480.
- Betapudi V, Licate LS, Egelhoff TT (2006) Distinct roles of nonmuscle myosin II isoforms in the regulation of MDA-MB-231 breast cancer cell spreading and migration. *Cancer Res* 66(9):4725–4733.
- Betapudi V, Gokulrangan G, Chance MR, Egelhoff TT (2011) A proteomic study of myosin II motor proteins during tumor cell migration. *J Mol Biol* 407(5):673–686.
- Heisenberg CP, Bellaiche Y (2013) Forces in tissue morphogenesis and patterning. *Cell* 153(5):948–962.
- Mahajan RK, Pardee JD (1996) Assembly mechanism of *Dictyostelium* myosin II: Regulation by K⁺, Mg²⁺, and actin filaments. *Biochemistry* 35(48):15504–15514.
- Niederman R, Pollard TD (1975) Human platelet myosin. II. In vitro assembly and structure of myosin filaments. *J Cell Biol* 67(1):72–92.
- Yumura S, et al. (2005) Multiple myosin II heavy chain kinases: Roles in filament assembly control and proper cytokinesis in Dictyostelium. *Mol Biol Cell* 16(9):4256–4266.
- Egelhoff TT, Lee RJ, Spudich JA (1993) Dictyostelium myosin heavy chain phosphorylation sites regulate myosin filament assembly and localization in vivo. *Cell* 75(2):363–371.
- Robinson DN, Cavet G, Warrick HM, Spudich JA (2002) Quantitation of the distribution and flux of myosin-II during cytokinesis. *BMC Cell Biol* 3:4.
- Murphy CT, Rock RS, Spudich JA (2001) A myosin II mutation uncouples ATPase activity from motility and shortens step size. *Nat Cell Biol* 3(3):311–315.
- Kee YS, et al. (2012) A mechanosensory system governs myosin II accumulation in dividing cells. *Mol Biol Cell* 23(8):1510–1523.
- Ren Y, et al. (2009) Mechanosensing through cooperative interactions between myosin II and the actin crosslinker cortexillin I. *Curr Biol* 19(17):1421–1428.
- Delpu Y, et al. (2011) Genetic and epigenetic alterations in pancreatic carcinogenesis. *Curr Genomics* 12(1):15–24.
- Sun Q, et al. (2014) Competition between human cells by entosis. *Cell Res* 24(11):1299–1310.
- Maitra A, et al. (2003) Global expression analysis of well-differentiated pancreatic endocrine neoplasms using oligonucleotide microarrays. *Clin Cancer Res* 9(16 Pt 1):5988–5995.
- Maitra A, et al. (2003) Multicomponent analysis of the pancreatic adenocarcinoma progression model using a pancreatic intraepithelial neoplasia tissue microarray. *Mod Pathol* 16(9):902–912.
- Tan MH, Chu TM (1985) Characterization of the tumorigenic and metastatic properties of a human pancreatic tumor cell line (ASPC-1) implanted orthotopically into nude mice. *Tumour Biol* 6(1):89–98.
- D'Apolito M, Guarneri V, Boncristiano M, Zelante L, Savoia A (2002) Cloning of the murine non-muscle myosin heavy chain IIA gene ortholog of human MYH9 responsible for May-Hegglin, Sebastian, Fechtner, and Epstein syndromes. *Gene* 286(2):215–222.
- Marini M, et al. (2006) Non-muscle myosin heavy chain IIA and IIB interact and co-localize in living cells: Relevance for MYH9-related disease. *Int J Mol Med* 17(5):729–736.
- Even-Ram S, Yamada KM (2007) Of mice and men: Relevance of cellular and molecular characterizations of myosin IIA to MYH9-related human disease. *Cell Adhes Migr* 13(3):152–155.
- Dupont S, et al. (2011) Role of YAP/TAZ in mechanotransduction. *Nature* 474(7350):179–183.
- Calvo F, et al. (2013) Mechanotransduction and YAP-dependent matrix remodelling is required for the generation and maintenance of cancer-associated fibroblasts. *Nat Cell Biol* 15(6):637–646.
- Liang S, et al. (2011) MicroRNA let-7f inhibits tumor invasion and metastasis by targeting MYH9 in human gastric cancer. *PLoS ONE* 6(4):e18409.
- Schramek D, et al. (2014) Direct in vivo RNAi screen unveils myosin IIA as a tumor suppressor of squamous cell carcinomas. *Science* 343(6168):309–313.
- Surcel A, Kee YS, Luo T, Robinson DN (2010) Cytokinesis through biochemical-mechanical feedback loops. *Semin Cell Dev Biol* 21(9):866–873.
- Luo T, Mohan K, Iglesias PA, Robinson DN (2013) Molecular mechanisms of cellular mechanosensing. *Nat Mater* 12(11):1064–1071.
- Luo T, et al. (2012) Understanding the cooperative interaction between myosin II and actin cross-linkers mediated by actin filaments during mechanosensation. *Biophys J* 102(2):238–247.
- Cross SE, Jin YS, Rao J, Gimzewski JK (2007) Nanomechanical analysis of cells from cancer patients. *Nat Nanotechnol* 2(12):780–783.
- Beynon KI, Hutson DH, Wright AN (1973) The metabolism and degradation of vinyl phosphate insecticides. *Residue Rev* 47:55–142.
- Ike M, Chen MY, Jin CS, Fujita M (2002) Acute toxicity, mutagenicity, and estrogenicity of biodegradation products of bisphenol-A. *Environ Toxicol* 17(5):457–461.
- Vallini G, Frassinetti S, D'Andrea F, Catelani G, Agnolucci M (2001) Biodegradation of 4-(1-nonyl)phenol by axenic cultures of the yeast *Candida aquatextoris*: Identification of microbial breakdown products and proposal of a possible metabolic pathway. *Int Biodegrad Biodegr* 47(3):133–140.
- Tanihata Y, Watanabe M, Mitsukura K, Maruyama K (2012) Oxidative degradation of 4-hydroxyacetophenone in *Arthrobacter* sp. TGJ4. *Biosci Biotechnol Biochem* 76(4):838–840.
- Choi DH, Lee YJ, Kim JS, Kang DG, Lee HS (2012) Cynanchum wilfordii ameliorates hypertension and endothelial dysfunction in rats fed with high fat/cholesterol diets. *Immunopharmacol Immunotoxicol* 34(1):4–11.
- Choi DH, et al. (2012) Improved endothelial dysfunction by Cynanchum wilfordii in apolipoprotein E(-/-) mice fed a high fat/cholesterol diet. *J Med Food* 15(2):169–179.
- Jiang Y, et al. (2011) Chemical constituents of Cynanchum wilfordii and the chemotaxonomy of two species of the family Asclepiadaceae, C. wilfordii and C. auriculatum. *Arch Pharm Res* 34(12):2021–2027.
- Dolara P, Vezzani A, Caderni G, Coppi C, Torricelli F (1993) Genetic toxicity of a mixture of fifteen pesticides commonly found in the Italian diet. *Cell Biol Toxicol* 9(4):333–343.
- Akashi T, Kanbe T, Tanaka K (1994) The role of the cytoskeleton in the polarized growth of the germ tube in *Candida albicans*. *Microbiology* 140(Pt 2):271–280.
- Hepler PK, Jackson WT (1969) Isopropyl N-phenylcarbamate affects spindle microtubule orientation in dividing endosperm cells of *Haemanthus katherinae* Baker. *J Cell Sci* 5(3):727–743.
- Magistrini M, Szöllösi D (1980) Effects of cold and of isopropyl-N-phenylcarbamate on the second meiotic spindle of mouse oocytes. *Eur J Cell Biol* 22(2):699–707.
- Oliver JM, Krawiec JA, Berlin RD (1978) A carbamate herbicide causes microtubule and microfilament disruption and nuclear fragmentation in fibroblasts. *Exp Cell Res* 116(1):229–237.
- Walker GM (1982) Cell cycle specificity of certain antimicrotubular drugs in *Schizosaccharomyces pombe*. *J Gen Microbiol* 128(1):61–71.
- Clayton L, Lloyd CW (1984) The relationship between the division plane and spindle geometry in *Allium* cells treated with CIPC and griseofulvin: An anti-tubulin study. *Eur J Cell Biol* 34(2):248–253.

Supporting Information

Surcel et al. 10.1073/pnas.1412592112

SI Discussion

Although 4-HAP's direct target remains to be identified, 4-HAP appears to work through myosin II as indicated by two key pieces of data. First, 4-HAP increases cortical tension in WT cells but not in *myosin II* null mutant cells (a complete genetic deletion; Fig. 3G). Second, 4-HAP does not have an effect on the S456L myosin II mutant, thus demonstrating a requirement for the full myosin II step (Fig. 4). Therefore, 4-HAP requires a full working myosin II for its effect on mechanics.

To decipher the requirements of 4-HAP on myosin II, a library of mutant myosin II proteins that affect each of the major aspects of myosin II function was used. The promotion of myosin II cortical localization by 4-HAP implied a possible effect on heavy-chain phosphorylation regulation of myosin II BTF assembly. To test this hypothesis, we used the two genetic mutants that mimic the phosphorylated (3xAsp, poor assembly mutant) and non-phosphorylated (3xAla, overassembly mutant) states. Treatment with 4-HAP still worked on these two mutants, demonstrating that its mechanism is independent of myosin heavy-chain phosphorylation (Fig. 4). This result is consistent with considerable published experimental and computational work (e.g., ref. 1).

Having ruled out a direct involvement of heavy-chain phosphorylation regulation, we turned to the motor domain. The S1 fragment (motor only) did not respond to 4-HAP. S1's non-response demonstrated that there is not a global nonspecific effect, such as a loss of membrane potential, that would cause the proton pump to stop producing ATP, thus leading the S1 motor to bind actin in the rigor state. Other treatments that deplete the cell of ATP also cause the S1 motor to bind to the cortex, which was not observed with 4-HAP treatment. Further, the S1 mutant data indicate that dimeric myosin II is essential for 4-HAP's effect, which is important for the mechanism of myosin II assembly.

Next, we tested the S456L uncoupler mutant myosin II. This mutation affects an amino acid in the switch II helix, which resides inside the motor domain. This mutant residue disrupts the communication between the ATP-binding pocket and the converter domain of the motor. The consequence of this mutation is that the motor has normal ATPase activity but uncoupled mechanochemistry. The mutant has been studied in detail for its biochemical kinetic properties and its mechanical properties (2). From these studies, it is known that the S456L myosin has two defects: a short 2-nm step size, which is one-quarter of the WT 8-nm step, and a threefold longer ADP-bound state than WT myosin II. Because the velocity of a motor is dependent on the step size divided by the strong actin-bound state time (generally dominated by the ADP-bound state under no-force conditions), this motor slides actin filaments at 1/10th [$\sim 1/(4 \times 3)$] of the WT velocity. The S456L mutant is insensitive to 4-HAP (Fig. 4).

This observation is enormously restrictive for what the cellular mechanism of 4-HAP can be. To explain why, we start with a molecular view of what the motor is doing. To begin, ATP binds the myosin II motor, which causes the motor to release from the actin filament. The motor rapidly hydrolyzes the ATP to ADP•P_i, and it is not until the motor encounters an actin filament that it releases the P_i. Upon encountering an actin filament, the motor binds weakly and then tightly as the P_i is released (cartoon in Fig. 4C). This initial actin interaction happens normally in S456L, which is why its V_{\max} of ATP hydrolysis is normal. The WT and S456L motors undergo an ~ 2 -nm step, at which point they have reached the isometric state. Here, WT and S456L diverge in what they do. WT extends the power stroke another 6 nm to

complete the full 8-nm step. Consequently, this larger step will lead to a bigger deformation in any compliant elements throughout the motor or BTF. However, S456L exits the normal pathway, where it does not take any larger step, waits a little longer before letting go of the ADP, ultimately rebinds ATP, and releases from the actin filament. Thus, the S456L mutant identifies a very specific place in the myosin II mechanochemical cycle that 4-HAP depends on for its ability to promote myosin II accumulation.

Moving up to the cortical actin network and whole cell, it is now important to consider how S456L works at these hierarchical levels. At the cellular level, S456L acts as though it is an inert, dead myosin II in the context of interphase cells that are not experiencing mechanical stress (3, 4). However, as soon as a mechanical stress propagates through the network, S456L behaves as though it is a WT myosin motor. This WT behavior is seen in two scenarios: cytokinesis furrow ingression (3) and when mechanical stress is imposed using aspiration (5, 6). Thus, physiological (cytokinesis) and imposed (aspiration) mechanical stresses rescue the activity of this mutant motor. Because S456L can accumulate in response to mechanical stress, it is implied that it can sample the isometric, cooperative binding state (1). Importantly, the force-dependent bond length of WT myosin II is ~ 1 –2 nm, which is similar to S456L's 2-nm step. Thus, 4-HAP must do something that depends on the remaining 6 nm of the WT step. We currently suspect 4-HAP helps stabilize directly or indirectly the stretching of another compliant element in the myosin II tail, which assists in another aspect of thick filament assembly. Applied mechanical stresses are able to stretch this element, even if the motor cannot exert enough deformation (S456L short step size) so long as the motor can enter the cooperative binding state. This crosstalk between the motor and the tail may be affected by 4-HAP.

Finally, myosin II accumulation occurs as a result of the function of a control system constructed by two feedback loops (7). The implication is that myosin II cortical accumulation depends on multiple signal inputs, which include integrated biochemical and mechanical signaling. If we break this control system at a key point by deleting cortexillin I, a specific membrane anchoring, actin cross-linking protein that cooperates with myosin II for accumulation in response to mechanical stress (5–7), we also block myosin II accumulation by 4-HAP (Fig. 4A and B and Fig. S7E and F). This result demonstrates that 4-HAP requires an intact control system for myosin II accumulation. If the 4-HAP-directed myosin II accumulation were nonspecific, one might expect that the accumulation would be independent of specific known pathways that the cell uses for myosin II accumulation during normal processes like cytokinesis.

SI Methods

CIMPAQ Work Flow. An overview of the primary screen, including CIMPAQ analysis, is presented in Fig. S1A.

Cell Strains and Culture. *Dictyostelium discoideum* strains used in this study are listed in Table S3. Cells grown for primary and secondary chemical screening were cultured in Hans' enriched HL-5 media [1.4XHL-5 enriched with 8% FM (8)] with penicillin and streptomycin at 22 °C in 384-well cyclo-olefin polymer (COP) plates (Aurora Biotechnologies). These plates were chosen for their optical characteristics that generated a tighter distribution of nuclei per cell counts, preferable to other plates we tested (Fig. S1B–D). All other cells were cultured in HL-5

medium with glucose (FORMEDIUM Ltd.) with penicillin and streptomycin at 22 °C on 10-cm Petri dishes (8) or grown in suspension in 200-mL flasks. The *myoII* null cells (9), *racE* null cells (10), *cortI* null cells (8), and *kif12* null cells (11) have been described previously. NLS-tdTomato was prepared by cloning the sequence in the pLD1A15SN expression plasmid (8). Transformation of all strains was achieved by electroporation using a Genepulser-II electroporator (Bio-Rad). Transformed cells were selected with 10–15 µg/mL G418, 15–50 µg/mL hygromycin, or both when two plasmids were transformed together. For drug treatment, cells were preincubated with 0.1% DMSO for 4 h before treatment.

A10.7 cells were grown according to standard cell culture methods in DMEM high glucose (Gibco) with 1% penicillin and streptomycin and 10% FBS on cell culture Petri dishes. HPDE and ASPC-1 cells were grown according to standard cell culture methods in Keratinocyte media (Gibco) with 1% penicillin and streptomycin or in RPMI 1640, L-Glutamine media (Gibco) supplemented with 1% penicillin and streptomycin, sodium pyruvate, 10% FBS, and 0.2% insulin, respectively. HL-60 cells were grown in RPMI supplemented with 1% antibiotic-antimycotic mix (Invitrogen), 25 mM Hepes (Invitrogen), and 20% FBS. For drug treatment, cells were preincubated with 0.1% DMSO overnight. In accordance with NIH guidelines, cell lines were authenticated using short tandem repeat profiling at the genetic resources core facility at Johns Hopkins University.

Primary and Secondary Chemical Library Screening. Ax3::NLS-tdTomato cells were plated on 384-well COP plates with a MicroFloSelect microplate dispenser (BioTek) at volumes of 80 µL, with a cell concentration of 1,000 cells per milliliter for the 24-h and 48-h time points and at the same volume with a cell concentration of 220 cells per milliliter for the 72-h time point. Each plate contained four rows of untreated cells with 0.2% DMSO. For the remaining wells, each small molecule maintained at the Johns Hopkins ChemCORE facility was added at 5 µM, with a final DMSO concentration of 0.2%. Almost half of the ChemBridge DIVERSet library, which is a 50,000-compound chemical diversity library, was screened over a 3-d period on a Becton Dickinson Pathway 855 Bio-imager System using a 20× objective (0.75 N.A.). Each image consisted of a montage of four images collected around the center of the well, resulting in a total size of 1,344 × 1,024 pixels per image. Secondary chemical screening was carried out in quadruplicate, with identical culturing conditions as in the primary screen. Stocks of each compound (14 mM) dissolved in 100% DMSO were diluted to the following final concentrations: 350 pM, 3.5 nM, 35 nM, 350 nM, 3.5 µM, and 35 µM.

CIMPAQ Processing, Analysis, and Hit Identification.

Image processing using CIMPAQ. Raw image files from both the primary and secondary screenings were processed through CIMPAQ (Fig. S1 E and F). The single-wavelength fluorescence images were converted from a 16-bit format to an eight-bit format. The MATLAB Image Processing Toolbox (MathWorks) was used to segment the images to identify the nuclei and cytoplasm. The number of nuclei within each segmented cell was quantified to produce a histogram of nuclei per cell for each image (Fig. S1G). All segmented cells that were coincident with the image edge were disregarded.

Image analysis using CIMPAQ. From the histogram of nuclei per cell count, the ratio of the number of multinucleate cells to the number of mononucleate cells and the ratio of the number of binucleate cells to the number of mononucleate cells were computed. Multinucleate cells are defined as cells that contain more than two nuclei. The distribution of both ratios across multiple wells was simultaneously visualized using a scatter plot, with the ratio of multinucleate cells to mononucleate cells plotted

on the *x* axis and the ratio of binucleate cells to mononucleate cells plotted on the *y* axis (Fig. S1 H and I). Other information, such as the average number of nuclei per cell, the mean nuclear area, and the normalized histogram with respect to total cell number, were also computed.

Hit identification using CIMPAQ. Compounds that generate an increase in the number of multinucleate (more than two nuclei per cell) cells are considered cytokinesis inhibitors. Because nearly all cultured cells, including *Dictyostelium*, have a low background (typically <5% for WT) of nonmononucleate cells, CIMPAQ spreads the data for each sample by determining the ratio (bi/mono) of binucleate (two nuclei per cell) to mononucleate cells and the ratio (multi/mono) of multinucleate (more than two nuclei per cell) to mononucleate cells. These two ratios then define a set of Cartesian coordinates, describing the effect of each compound on a given cell line. The coordinates for each compound are plotted on a 2D graph. CIMPAQ fits the control data to a 2D Gaussian distribution (Fig. S1H) and determines the contour lines for 2 SDs (2SD), 3SD, etc. from the control mean (Fig. S1I). Hit compounds are rank-ordered based on how many SDs away they are from the untreated wells.

To fit the nuclei per cell ratios, we used the MATLAB Statistics and Optimization Toolboxes and fitted the ratios data from the control wells with a bivariate Gaussian function. The fitted parameters of the Gaussian function were used to assign a metric number to each sample well. The metric number is defined as the value of the Gaussian function when evaluated at the ratio values computed for a sample well of interest:

$$\text{metric number} = f(\text{ratio multi/mono}_{\text{sample}}, \text{ratio bi/mono}_{\text{sample}}) \\ \text{where } f(x,y) = \text{fitted Gaussian function.}$$

Based on the definition, a smaller metric number corresponds to larger deviations of the ratio pair from the control mean ratios. The cutoff for a well to be considered a hit was that the ratio pair had to be >2SD from the control mean ratios. All identified hits were further categorized by the number of SDs away from the control mean ratios.

To assess the efficacy of CIMPAQ in identifying cytokinesis inhibitors, a 384-well plate containing primarily the AX3::NLS-tdTomato cell line was randomly seeded with *cortexillin I* null (a cytokinesis mutant) cells transformed with the NLS-tdTomato construct. CIMPAQ was able to identify 86% of the *cortexillin I*-containing wells (Fig. S24).

Mitotic inhibitors. Early mitotic inhibitors were identified using a simple threshold value, where the average nuclear area is greater than 28 pixels. Untreated WT control cells had a tight nuclear area of 22 pixels. This threshold value reliably identified cells treated for 24 h and 48 h with 5 µM and 10 µM nocodazole, a known microtubule destabilizing agent (Fig. S2 C–E).

Lethal compounds. Lethal compounds were identified based on the total number of cells detected in the acquired image. Wells that had significantly fewer cells compared with the control (>2SD difference, typically 10% of the average number of cells from all untreated wells) were counted as wells that contain a lethal compound at the concentration of 5 µM used in the primary screening. Because data were collected over 3 d, growth inhibitors were also identified using similar metrics.

Library testing of CIMPAQ. To test CIMPAQ, original pilot screens were performed on two BIOMOL libraries (Enzo Life Sciences): 84 protein kinase inhibitors and 70 ion channel inhibitors (data summary of hits from these collections is provided in Tables S1 and S2, and sample CIMPAQ output is illustrated in Fig. S2B). In each of these setups, manual counts were compared with CIMPAQ-generated numbers. Overall, nuclei from over 50,000 cells were manually counted for cross-validation of the CIMPAQ software.

Imaging and Image Analysis. Imaging conditions during the primary screen are described above. All other image analysis was performed as previously described (7). *Dictyostelium* cells were transferred from Petri dishes (with 0.1% DMSO incubation in growth media of 4 h) to imaging chambers and allowed to adhere for 20 min in growth media with 0.1% DMSO. After the cells adhered, the growth media were replaced with MES starvation buffer [50 mM MES (pH 6.8), 2 mM MgCl_2 , 0.2 mM CaCl_2] with 0.1% DMSO.

Confocal imaging was performed on a Zeiss 510 Meta microscope with a 63 \times (1.4 N.A.) objective (Carl Zeiss). Epi-fluorescence and TIRF imaging was performed in a 22 $^{\circ}\text{C}$ temperature-controlled room with an Olympus IX81 microscope using a 40 \times (1.3 N.A.) or 60 \times (1.49 N.A.) objective and a 1.6 \times optovar (Olympus), as previously described. Image analysis was performed with ImageJ (rsb.info.nih.gov/ij). Many datasets were independently analyzed by multiple investigators.

MPA Assay, Cortical Tension Measurements, and Creep Tests. The instrumental and experimental setups have been described previously (12, 13). MPA assays were all carried out in growth media with 0.1% DMSO. For cortical tension measurements of *Dictyostelium* cells, pressure was applied to the cell cortex with a micropipette (2- to 3- μm radius; R_p) to the equilibrium pressure (ΔP), where the length of the cell inside the pipette (L_p) was equal to R_p . The effective cortical tension (T_{eff}) was calculated by applying the Young–Laplace equation: $\Delta P = 2T_{\text{eff}}(1/R_p - 1/R_c)$, where R_c is the radius of the cell and ΔP is the equilibrium pressure when $L_p = R_p$ (14, 15). For creep tests on mammalian strains, a constant aspiration stress was applied over 60 s. The R_p was 3.5–4.5 μm . For quantification, the L_p/R_p ratio value was measured every 2 s and plotted as a function of time. A10.7 and HEK 293 cells could only be aspirated at a low pressure range (0.15 $\text{nN}/\mu\text{m}^2$), whereas HPDE, ASPC-1, and HL-60 cells could be aspirated at higher pressure ranges (0.25 $\text{nN}/\mu\text{m}^2$) because they were stiffer.

Sedimentation Assay.

Dictyostelium sedimentation protocol. The sedimentation protocol was modified from the method of Yumura et al. (16). A total of 1.5×10^6 cells were pelleted for 5 min at $400 \times g$. The pellet was washed in MES starvation buffer [50 mM MES (pH 6.8), 0.2 M CaCl_2 , 2 mM MgCl_2] and then resuspended in buffer A [0.2 M MES (pH 6.8), 2.5 mM EGTA, 5 mM MgCl_2 , 0.5 mM ATP] and incubated on ice for 5 min. An equal volume of buffer B (buffer A + 1% Triton X-100 + protease inhibitor mixture) was added, and the samples were vortexed for 5 s, followed by 5 min of incubation on ice. After a $10,000 \times g$ spin for 2 min at 4°C , the supernatant was transferred to a fresh tube. The Triton-insoluble pellet was dissolved in 50 μL of sample buffer and heated for 5 min at 100°C . A twofold volume of -20°C acetone was added to the supernatant, which was subsequently incubated on ice for 10 min and then centrifuged at $10,000 \times g$ for 10 min at 4°C . The Triton-soluble fraction was dissolved in 50 μL of sample buffer and heated for 5 min at 100°C . Samples were loaded on a 15% SDS/polyacrylamide gel.

Mammalian cell sedimentation protocol. The sedimentation protocol was adapted from the protocol described above. A total of 3×10^6 cells were pelleted for 5 min at $400 \times g$ and washed in 1 mL of PBS. The pellet was resuspended in 100 μL of lysis buffer [50 mM 1,4-piperazine diethane sulfonic acid (pH 6.8), 46 mM NaCl, 2.5 mM EGTA, 1 mM MgCl_2 , 1 mM ATP, 0.5% Triton X-100, and protease inhibitor mixture (PMSF, N- α -tosyl-L-lysine chloromethyl ketone hydrochloride, aprotinin)]. Samples were vortexed briefly and incubated on ice for 20 min, followed by centrifugation at $15,000 \times g$ for 5 min at 4°C . The pellet was resuspended in 100 μL of lysis buffer minus Triton X-100, and both the pellet and supernatant fractions were heated to 100°C

for 3 min with RNaseA. Samples were incubated at 37°C for 30 min and then heated to 100°C in sample buffer for 5 min. Samples were loaded on a 15% SDS/polyacrylamide gel. Western blot analyses of phosphomyosin IIA were performed on whole-cell lysates of cells treated as above in lysis buffer with 10 mM NaF.

Assembly Assay.

Protein purification. Bacterial expression plasmids coding for an N-terminal 6 \times His tag, fused to the mCherry fluorophore and to the assembly domains of *Dictyostelium* myosin II (residues 1,533–1,823), MYH9 (residues 1,722–1,960), or MYH10 (residues 1,729–1,976), were generated using standard cloning techniques. *Dictyostelium* 14-3-3 was also expressed in bacteria as a 6 \times His-tagged fusion protein (17). Proteins were expressed in BL-21 Star (DE3; Invitrogen) *Escherichia coli* in LB shaking culture overnight at room temperature. Bacteria were harvested by centrifugation and lysed by lysozyme treatment followed by sonication, and the lysate was clarified by centrifugation. Polyethyleneimine (PEI) was added to a final concentration of 0.1% to precipitate nucleic acids, which were then removed by centrifugation. The *Dictyostelium* 14-3-3 precipitated in the PEI pellet, which was resuspended in column running buffer [10 mM Hepes (pH 7.1), 500 mM NaCl, 10 mM imidazole], clarified by centrifugation and filtration, and run on a nickel-nitrilotriacetic (Ni-NTA) acid metal affinity column to obtain high-purity 14-3-3. The myosin constructs remained in the PEI supernatant and were precipitated by adding ammonium sulfate to 50% saturation and centrifuging. The pellet was resuspended in column running buffer and run on a Ni-NTA metal affinity column, followed by a sizing column. Protein purity was verified by SDS/PAGE followed by Coomassie Blue staining, and concentration was quantified by UV absorbance using the calculated extinction coefficient for each protein's amino acid sequence.

Assembly assay. In vitro assembly of myosin was conducted according to the method of Zhou et al. (17), with a number of modifications. The protein concentration for each species in the tube was increased to 1 μM to ensure that the smaller protein was adequately visible by Coomassie Blue staining, and the incubation time and temperature were adjusted to 30 min at the physiological temperature for each myosin species (22°C for *Dictyostelium* myosin, 37°C for human myosins). These temperatures were also used during the centrifugation step.

Motility Assay. The chicken nonmuscle IIB (NMIIB) heavy meromyosin construct (residues 1–1,228, GenBankTM accession no. M93676, no splice insert) was purified as previously described (18). Motility assays were performed at 22°C and imaged on a Zeiss Axiovert 200 microscope with an Andor Luca camera. The flow cells were constructed using a glass slide, two pieces of double-sided tape, and a nitrocellulose-coated coverslip. Flow cells were incubated with 0.05 mg/mL GFP antibodies [MP Biomedicals; 0.05 mg/mL in assay buffer (AB) without DTT: 25 mM KCl, 25 mM imidazole-HCl (pH 7.5), 1 mM K-EGTA, 4 mM MgCl_2 ; 2-min incubation time], followed by a BSA block (1 mg/mL in AB as above with 10 mM DTT, 6-min incubation time). NMIIB was added to the flow cell at a concentration of 420 nM and incubated for 2 min. The flow cell was rinsed with AB and then incubated for 2 min with 50 nM F-actin in AB, stabilized with TRITC-phalloidin (American Peptide Company). The flow cell was washed again with AB. Finally, motility buffer was added and actin filaments were visualized. Motility buffer for “none” (control) contained 2 mM ATP, 2 mM free Mg^{2+} , 0.086 mg/mL glucose oxidase, 0.014 mg/mL catalase, and 0.09 mg/mL glucose in AB. Motility buffers with compounds contained 0.0036% (vol/vol) DMSO; 500 nM 4-HAP; 500 nM 3,4-DCA, or 250 nM 4-HAP; and 250 nM 3,4-DCA as indicated for each experiment.

Chemistry.

Synthesis of 4-acetylphenyl (3,4-dichlorophenyl)carbamate. To a mixture of 4-HAP (250 mg, 1.8 mmol) in dichloromethane (4.6 mL) at room temperature was added 3,4 dichlorophenyl isocyanate (380 mg, 2.0 mmol) in one portion, followed by addition of *N,N*-diisopropylethylamine (iPr₂NEt) (32 μ L, 0.18 mmol) in one portion. A white precipitate formed immediately upon addition of iPr₂NEt. Dichloromethane (2 mL) was added to enable more efficient stirring of the thick white mixture. The reaction was complete within 1 h as determined by TLC analysis. The reaction mixture was partitioned between water and chloroform in a separatory funnel, and the aqueous layer was extracted with chloroform (3 \times 10 mL). Organic layers were combined and dried over sodium sulfate. Purification of carbamate-7 was carried out on a Grace Reveleris flash chromatography system using a linear gradient (100% hexanes \rightarrow 100% ethyl acetate). The carbamate product precipitated from fractions and was collected for NMR characterization. ¹H NMR analysis in methanol-d₄ indicated that the isolated carbamate (129 mg, 20%) is identical to commercial carbamate-7 (ChemBridge) in all respects [¹H NMR (500 MHz, methanol-d₄) δ 7.84–7.94 (m, 2H), 7.73 (d, *J* = 2.04 Hz, 1H), 7.39 (d, *J* = 8.80 Hz, 1H), 7.32 (dd, *J* = 2.52, 8.80 Hz, 1H), 6.77–6.88 (m, 2H), 2.52 (s, 3H)]. Abbreviations as follows: d₄, deuteriums; m, multiplet; d, doublet; H, hydrogen; *J*, coupling constant; dd, doublet of doublets; s, singlet.

Degradation of carbamate-7 (5180622) in DMSO. Upon standing in methanol, the product obtained above degraded within 2.5 h as determined by TLC analysis. Degradation appeared more rapid in DMSO, the solvent used to generate stock solutions for biological evaluation. Thus, carbamate-7 obtained either by chemical synthesis or commercially from ChemBridge was dissolved in DMSO (1 mg/mL), and a time course to study its degradation was initiated immediately upon solvation. To stop the degradation reaction such that the product distribution could be captured at early time points, aliquots (40 μ L) were rapidly frozen into Eppendorf tubes incubating on dry ice. HPLC analysis on a Beckman Coulter HPLC System Gold Nouveau was performed on each sample immediately upon thawing. Carbamate-7 (5180622) degradation products were eluted at 3 mL \cdot min⁻¹ from a Grace Alltima C18 column (length = 53 mm,

i.d. = 7 mm, particle size = 3 μ M) over a linear gradient [5:95 acetonitrile/100 mM NH₄OAc (pH 6.8) to 100% 100 mM NH₄OAc (pH 6.8) over 15 min]. An HPLC stack plot depicting carbamate-7 degradation over time (Fig. S3B) is displayed at 254 nm. Synthetic and commercial carbamate-7 exhibit identical reactivity in DMSO to give 4-HAP, 3,4-DCA, and *N,N*-Bis(3,4-dichlorophenyl)urea (Fig. S3A). Comparison of the urea product and authentic *N,N*-Bis(3,4-dichlorophenyl) urea was performed using a linear gradient [5:95 acetonitrile/100 mM NH₄OAc (pH 6.8) to 100% 100 mM NH₄OAc (pH 6.8) over 5 min]. The urea was also confirmed by MS analysis using a Thermo Scientific TSQ Vantage triple quadrupole mass spectrometer interfaced with a Dionex UltiMate 3000 LC System. Parent mass analysis and isotopic distribution of the urea were confirmed by direct infusion for Q1 analysis in negative ion mode. Confirmation of the urea was further confirmed via characteristic fragmentation patterns determined using product ion (MS/MS) analysis monitoring in negative ion mode (Fig. S3C).

Migration Assay. Cells were starved with serum-reduced media for 24 h, harvested from flasks with trypsin/EDTA, washed with media containing 1% FBS, and resuspended at a cell density of 2–5 \times 10⁵ cells per milliliter. Cells (in 0.2 mL volume) were placed in the upper chamber of transwell (BD Biosciences), with 20% FBS-containing media in the lower well, and incubated at 37 $^{\circ}$ C for 24 h. Both sides of the transwell contained 4-HAP at the appropriate concentration, with a final DMSO concentration at 0.0025%. The transwells were MeOH-fixed and stained with 0.5% crystal violet for 20 min, followed by counting from six random microscopic fields.

Invasion Assay. Cells were treated as in the migration assay but were plated in transwells containing 2 mg/mL Matrigel (BD Biosciences).

Statistical Analyses. Datasets were collected and analyzed using KaleidaGraph (Synergy SoftwareA). ANOVA or Student *t* tests were performed using KaleidaGraph. For all experiments, *P* values <0.05 were considered significant, and calculated *P* values are included on the graphs, in the text, and/or in the figure legends.

- Luo T, et al. (2012) Understanding the cooperative interaction between myosin II and actin cross-linkers mediated by actin filaments during mechanosensation. *Biophys J* 102(2):238–247.
- Murphy CT, Rock RS, Spudich JA (2001) A myosin II mutation uncouples ATPase activity from motility and shortens step size. *Nat Cell Biol* 3(3):311–315.
- Reichl EM, et al. (2008) Interactions between myosin and actin crosslinkers control cytokinesis contractility dynamics and mechanics. *Curr Biol* 18(7):471–480.
- Girard KD, Kuo SC, Robinson DN (2006) Dictyostelium myosin II mechanosensitivity promotes active behavior of the cortex on long time scales. *Proc Natl Acad Sci USA* 103(7):2103–2108.
- Ren Y, et al. (2009) Mechanosensing through cooperative interactions between myosin II and the actin crosslinker cortexillin I. *Curr Biol* 19(17):1421–1428.
- Luo T, Mohan K, Iglesias PA, Robinson DN (2013) Molecular mechanisms of cellular mechanosensing. *Nat Mater* 12(11):1064–1071.
- Kee YS, et al. (2012) A mechanosensory system governs myosin II accumulation in dividing cells. *Mol Biol Cell* 23(8):1510–1523.
- Robinson DN, Spudich JA (2000) Dynacortin, a genetic link between equatorial contractility and global shape control discovered by library complementation of a Dictyostelium discoideum cytokinesis mutant. *J Cell Biol* 150(4):823–838.
- Ruppel KM, Spudich JA (1995) Myosin motor function: Structural and mutagenic approaches. *Curr Opin Cell Biol* 7(1):89–93.
- Gerald N, Dai J, Ting-Beall HP, De Lozanne A (1998) A role for Dictyostelium racE in cortical tension and cleavage furrow progression. *J Cell Biol* 141(2):483–492.
- Lakshmikanth GS, Warrick HM, Spudich JA (2004) A mitotic kinesin-like protein required for normal karyokinesis, myosin localization to the furrow, and cytokinesis in Dictyostelium. *Proc Natl Acad Sci USA* 101(47):16519–16524.
- Effler JC, et al. (2006) Mitosis-specific mechanosensing and contractile-protein redistribution control cell shape. *Curr Biol* 16(19):1962–1967.
- Kee Y-S, Robinson DN (2013) Micropipette aspiration for studying cellular mechanosensory responses and mechanics. *Methods Mol Biol* 983:367–382.
- Derganc J, Bozic B, Svetina S, Zeks B (2000) Stability analysis of micropipette aspiration of neutrophils. *Biophys J* 79(1):153–162.
- Octaviani E, Effler JC, Robinson DN (2006) Enlazin, a natural fusion of two classes of canonical cytoskeletal proteins, contributes to cytokinesis dynamics. *Mol Biol Cell* 17(12):5275–5286.
- Yumura S, et al. (2005) Multiple myosin II heavy chain kinases: Roles in filament assembly control and proper cytokinesis in Dictyostelium. *Mol Biol Cell* 16(9):4256–4266.
- Zhou Q, et al. (2010) 14-3-3 coordinates microtubules, Rac, and myosin II to control cell mechanics and cytokinesis. *Curr Biol* 20(21):1881–1889.
- Norstrom MF, Smithback PA, Rock RS (2010) Unconventional processive mechanics of non-muscle myosin IIB. *J Biol Chem* 285(34):26326–26334.

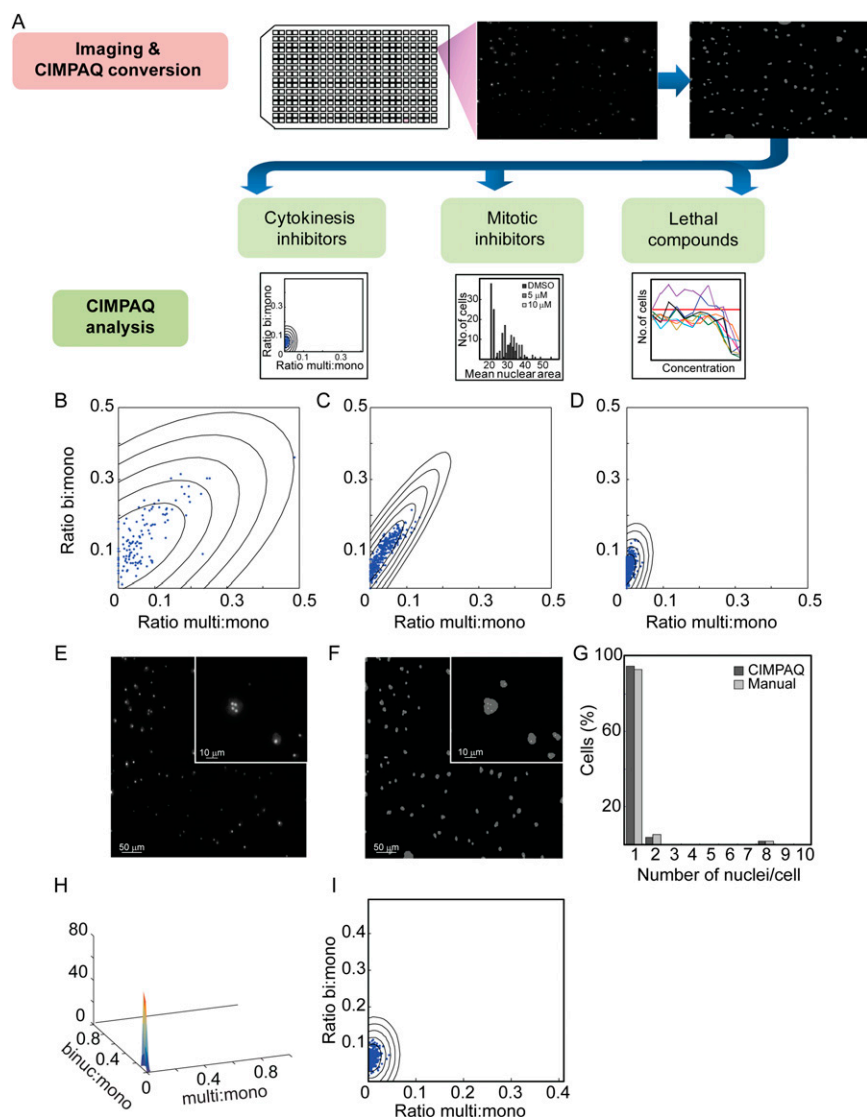


Fig. S1. CIMPAQ processes high-throughput data and identifies cytokinesis inhibitors. (A) Overview work flow diagram of primary screening from 384-well plating, to raw data acquisition, to CIMPAQ image conversion by segmentation. CIMPAQ analyzes the segmented data to identify and rank-order cytokinesis inhibitors, mitotic inhibitors, and lethal compounds. Plate type affects screening quality. Primary pilot screening was performed on COP plates (D), which showed a tighter distribution of multinucleate cells to mononucleate cells, as well as a tighter distribution of binucleate cells to mononucleate cells, compared with 96-well (B) and 384-well (C) Corning plates. The tighter distribution of untreated WT wells allowed for cytokinesis hits to be more readily identified in the following process: acquisition of raw images of NLS-tdTomato-expressing cells (E) and conversion into the CIMPAQ-processed version (F). In both E and F, the white box represents a zoomed quadrant, highlighting both the nuclear and cellular boundaries of a multinucleate (four nuclei per cell) and several mononucleate cells. (G) Sample histogram of a single well showing the distribution of nuclei per cell counts demonstrating high agreement between manual counts and CIMPAQ analysis. Over 50,000 cells have been manually counted to cross-compare with CIMPAQ output. (H) Cartesian coordinates defined by the ratio of binucleate (two nuclei per cell) to mononucleate cells and the ratio of multinucleate (more than two nuclei per cell) to mononucleate cells of the untreated WT wells are fitted to a 2D Gaussian distribution. (I) From this distribution, contour lines for all SDs from the control mean are determined for a given plate. Each blue dot represents one untreated control well from a 384-well plate. bi, binucleate; mono, mononucleate; multi, multinucleate.

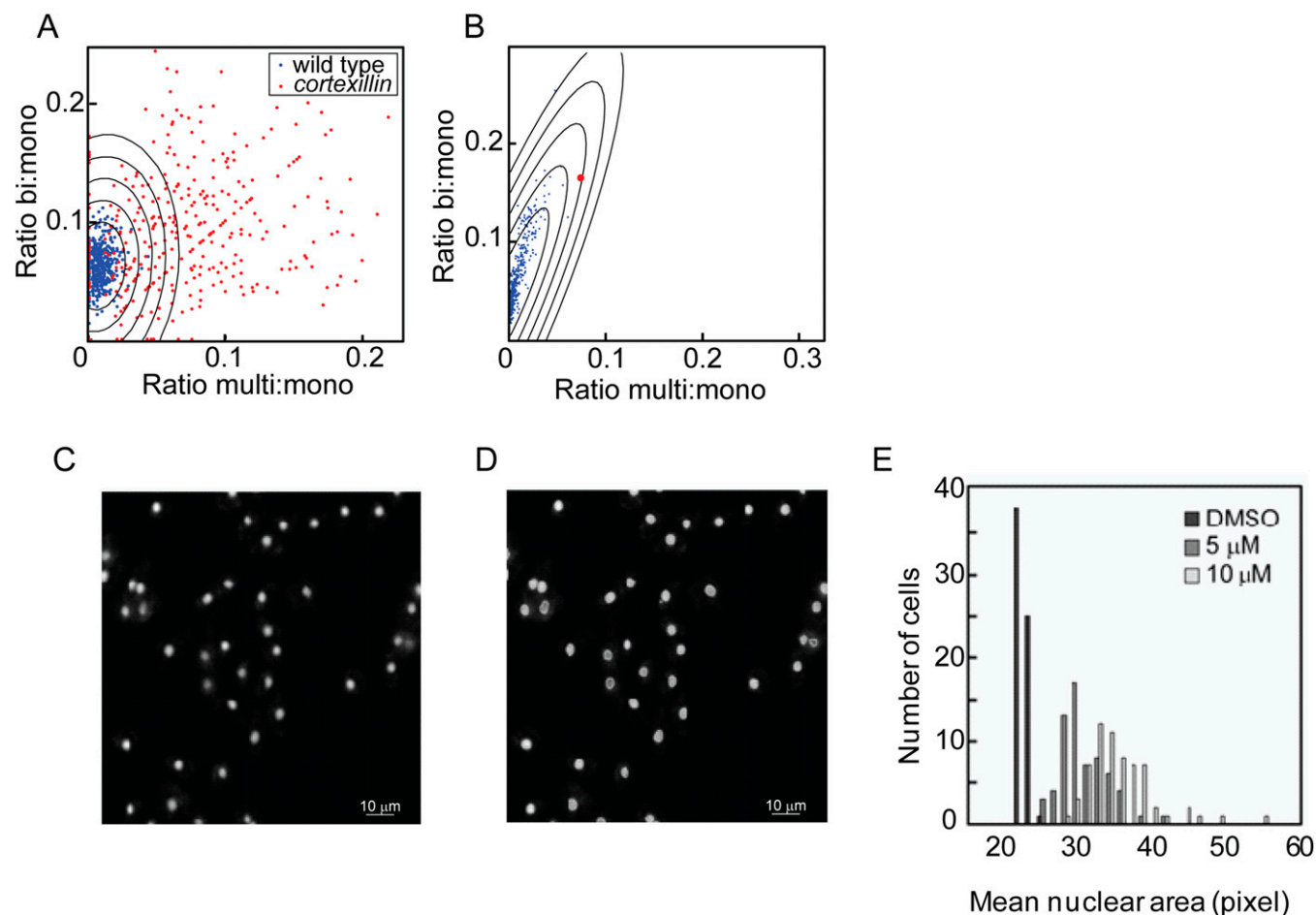


Fig. S2. Validation of CIMPAQ efficiency for cytokinesis and mitotic inhibitors. (A) CIMPAQ identified 86% of wells plated with *cortexillan I* null cells, which are deficient in cytokinesis (*cortI* null wells, red; WT wells, blue). (B) Sample CIMPAQ plot of hit compound (red) from the primary screen of the BIOMOL kinase library, which is ranked 4SDs away from the control data (blue). (C–E) CIMPAQ uses a threshold value for nuclear area to identify mitotic inhibitors. Raw images of 10 μ M nocodazole-treated cells (C) are processed by CIMPAQ (D). (E) CIMPAQ uses a simple threshold of 28 pixels for the mean nuclear area to identify early mitotic inhibitors. Distributions of the nuclear area of untreated cells (dark gray), 5 μ M nocodazole-treated cells (medium gray, middle), and 10 μ M nocodazole-treated cells (light gray) are shown.

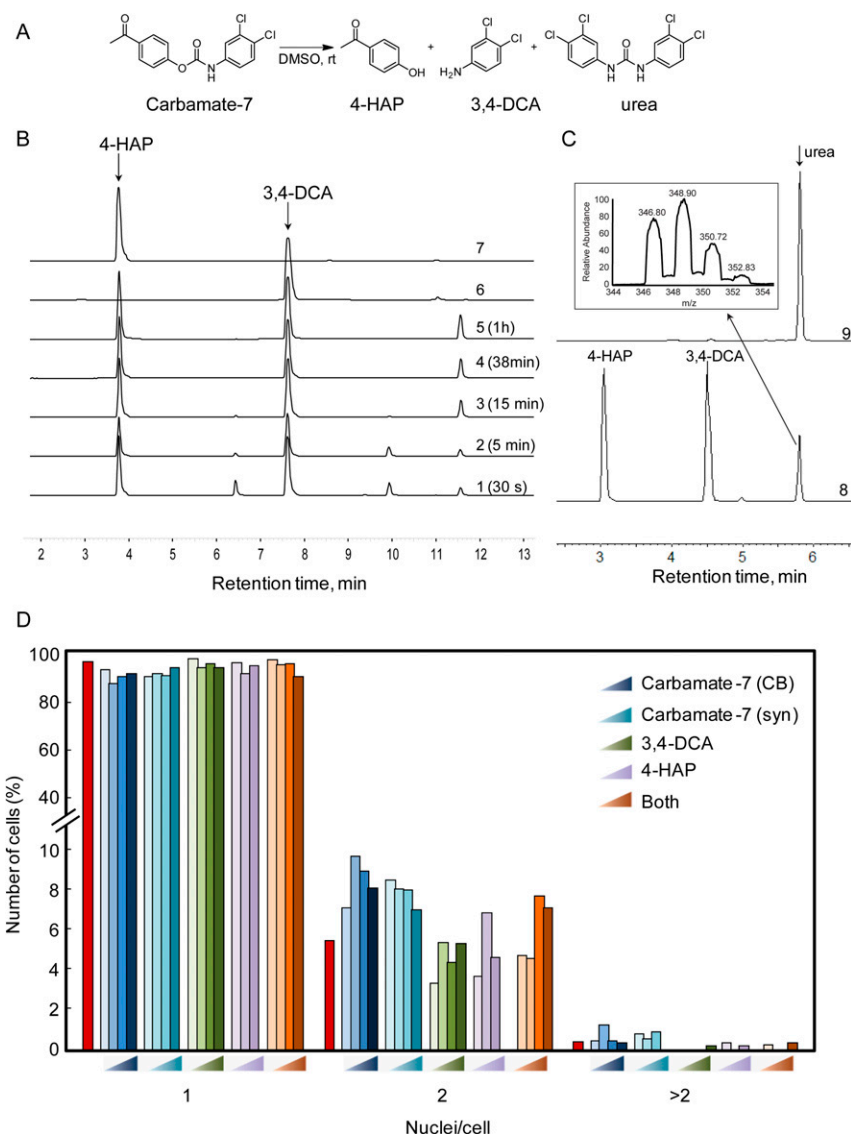


Fig. S3. Characterization of carbamate-7 degradation. (A) Degradation of carbamate-7 produces 3,4-DCA, 4-HAP, and *N,N'*-bis(3,4-dichlorophenyl)urea (urea). (B) HPLC stack plot showing degradation of synthetic (1–4) and commercial (5) carbamate-7 in DMSO, and comparison of degradation products and authentic 3,4-DCA (6) and 4-HAP (7). (C) Comparison of the urea degradation product (8) and authentic *N,N'*-bis(3,4-dichlorophenyl)urea (9) by HPLC analysis. (C, *Inset*) Presence of the urea was also confirmed by MS analysis, which shows the characteristic isotopic distribution for *N,N'*-bis(3,4-dichlorophenyl)urea. (D) Full nuclei per cell distribution of carbamate-7 and breakdown products. Together, 3,4-DCA and 4-HAP show an increase in binucleates and a decrease in mononucleates, consistent with the results from carbamate-7 treatment. CB, ChemBridge; syn, synthesized. Compound concentrations: 1 nM, 500 nM, 1,000 nM, 5,000 nM. At a concentration of 5,000 nM, 4-HAP was lethal, and is therefore not shown ($n = 400$ –1,441 cells per condition).

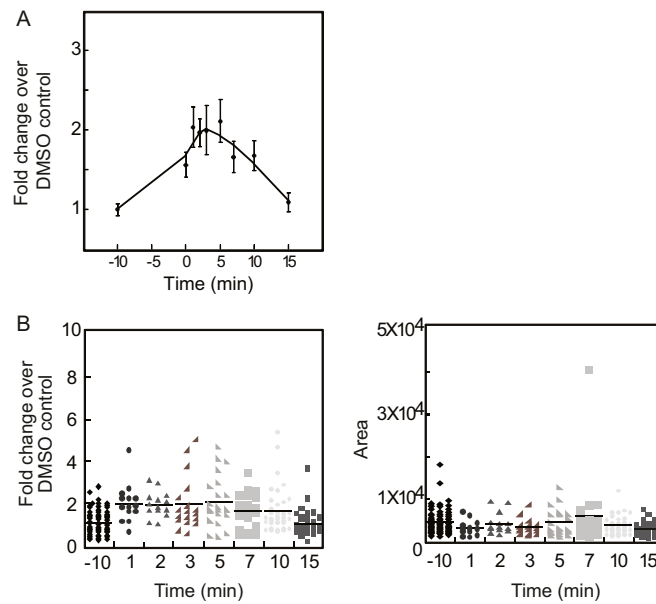


Fig. S4. Reversibility of 4-HAP effect on myosin II cortical enrichment. (A) Cells treated with 500 nM 4-HAP had a twofold increase in myosin II localization at the cortex by TIRF imaging within 10 min. At a concentration of 500 nM, 4-HAP was added at $t = -10$ min. When the 4-HAP-containing media was removed ($t = 0$), myosin II localization reverted to pretreatment levels within 15 min of removal ($n = 20$ –26 cells per time point). (B) Dot plot of the raw data shows the fold change over the DMSO control at each time point of the washout experiment (Left), and a dot plot of the raw data of the cell-surface contact area for the washout experiments shows no change in surface area among the time points (Right).

Table S1. CIMPAQ hits identified from the kinase inhibitor collection

Phenotypic categorization	CAS number	Name	Pathway affected
Cytokinesis inhibitors (nonlethal)	24386-93-4	5-Iodotubercidin	Inhibits ERK2, adenosine kinase, CK1, CK2, and insulin receptor kinase
Cytokinesis inhibitors (lethal, 5 d)	62004-35-7	LFM-A13	Tyrosine kinase inhibitor
	220904-83-6	GW 5074	A benzylidene oxindol derivative that inhibits the Raf/MEK/ERK2 kinase cascade by blocking the kinase activity of c-Raf1
	446-72-0	Genistein	Isoflavin that inhibits tyrosine kinase and has been previously reported to inhibit cytokinesis
	63177-57-1	Erbstatin analog	EGF receptor tyrosine kinase inhibitor; known IC ₅₀ (0.5 µg/mL); efficiently delays onset of EGF-induced DNA synthesis
	4452-06-6	ZM 449829	JAK-3 tyrosine kinase inhibitor; binds competitively to Jak3 ATP site; inhibits STAT-5 phosphorylation and T-cell proliferation
Lethal at 5 µM	167869-21-8	PD-98059	MAP kinase inhibitor
	10537-47-0	Tyrphostin 9	PDGF receptor tyrosine kinase
	172889-26-8	PP1	Src family tyrosine kinase inhibitor
	134036-53-6	AG-370	PDGF receptor kinase inhibitor
	548-04-9	Hypericin	Protein kinase C inhibitor
Lethal at 10 µM		2-Hydroxy-5-(2,5-dihydroxy benzylamino) benzoic acid	Inhibits CAM kinase II, EGF receptor tyrosine kinase, and pp60 kinase
	6865-14-1	Palmitoyl-DL-carnitine Cl	PKC inhibitor

AG-370, 3-amino-4-(1H-indol-5-ylmethylene)-2-pentenetricarbonitrile; CAM, calcium/calmodulin-dependent protein; CK, casein kinase; c-Raf1, rapidly accelerated fibrosarcoma serine/threonine-protein kinase; GW 5074, 3-(3,5-Dibromo-4-hydroxy-benzylidene)-5-iodo-1,3-dihydro-indol-2-one; LFM-A13, 2-Cyano-N-(2,5-dibromophenyl)-3-hydroxy-2-butenamide; MEK, mitogen/extracellular signal-regulated kinase; PD-98059, 2-(2-Amino-3-methoxyphenyl)-4H-1-benzopyran-4-one; PP1, 1-(1,1-Dimethylethyl)-1-(4-methylphenyl)-1H-pyrazolo[3,4-d]pyrimidin-4-amine; ZM 449829, 1-(2-Naphthalenyl)-2-propen-1-one.

Table S2. CIMPAQ hits identified from the ion channel inhibitor collection

Phenotypic categorization	CAS number	Name	Pathway affected
Cytokinesis inhibitors (nonlethal)	6151-40-2	Quinidine	Sodium channel blocker
	21306-56-9	QX-314	Sodium channel blocker
	29094-61-9	Glipizide	Potassium channel blocker
	113558-89-7	E-4031	Potassium channel blocker
	54527-84-3	Nicardipine	Calcium channel blocker
Cytokinesis inhibitors (lethal, 5 d)	2062-78-4	Pimozide	Calcium channel blocker
	107254-86-4	NPPB	Miscellaneous channel blocker
	52665-69-7	Antibiotic A-23187	Intracellular calcium blocker
Lethal at 5 µM	130495-35-1	SKF-96365	Calcium channel blocker
	74764-40-2	Bepridil	Calcium channel blocker
	113317-61-6	Niguldipine	Calcium channel blocker

NPPB, 5-Nitro-2-(3-phenylpropylamino)benzoic acid; QX-314, N-(2,6-Dimethylphenylcarbamoylmethyl)triethylammonium bromide; SKF-96365, 1-[2-(4-Methoxyphenyl)-2-[3-(4-methoxyphenyl)propoxy]ethyl]imidazole, 1-[β-(3-(4-Methoxyphenyl)propoxy)-4-methoxyphenethyl]-1H-imidazole hydrochloride.

Strain	Genotype	Experimental applications
WT control	Ax3(Rep orf ⁺)	Compound testing, MPA
Ax3::NLS-tdTomato	Ax3(Rep orf ⁺)::NLS-tdTomato, G418 ^R pLD1	Compound testing
<i>cort1</i> ¹¹⁵¹	<i>cort1</i> ¹¹⁵¹ (HS1151)	CIMPAQ testing
<i>race</i>	Δ <i>racE</i>	Compound testing
<i>myoII</i>	<i>myoII</i> (HS1)	Compound testing, MPA, Western blot
<i>kif12</i>	<i>kif12</i> (Rep orf ⁺)	Compound testing
<i>myoII</i> ::GFPmyoII; RFPtub	<i>myoII</i> (HS1)::GFPmyoII, G418 ^R :pBIG; RFP- α -tubulin, Hyg ^R :pDRH	SIM, TIRF, compound testing, sedimentation assay, MPA
<i>myoII</i> ::GFP3XAsp; RFPtub	<i>myoII</i> (HS1)::GFP3XAsp, G418 ^R :pBIG; RFP- α -tubulin, Hyg ^R :pDRH	TIRF, compound testing
<i>myoII</i> ::GFP3XAla; RFPtub	<i>myoII</i> (HS1)::GFP3XAla, G418 ^R :pBIG; RFP- α -tubulin, Hyg ^R :pDRH	TIRF, compound testing
<i>myoII</i> ::GFP5456L; RFPtub	<i>myoII</i> (HS1)::GFP5456L, G418 ^R :pBIG; RFP- α -tubulin, Hyg ^R :pDRH	TIRF, compound testing
<i>myoII</i> ::GFP51; RFPtub	<i>myoII</i> (HS1)::GFP51, G418 ^R :pBIG; RFP- α -tubulin, Hyg ^R :pDRH	TIRF, compound testing
<i>cort1</i> ¹¹⁵¹ ::GFPmyoII; RFPtub	<i>cort1</i> ¹¹⁵¹ (HS1151)::GFPmyoII, G418 ^R :pBIG; RFP- α -tubulin, Hyg ^R :pDRH	TIRF, compound testing

Hyg, hygromycin; pBIG, pDRH, and pLD1, *Dictyostelium* expression plasmids; ^R, resistance; Rep, replicase open reading frame; RFPtub, red fluorescent protein-tubulin; SIM, structured illumination microscopy.